AGU Advances

Key Points:

- Automated fault detections in seismic reflection data localize around the active main fault strand with well-defined average distributions
- Along strike variations in lateral extent of damage are best explained by fault obliquity
- Seafloor seeps correlate to areas of faulting and reduced sediment thickness

Correspondence to:

T. Alongi,
travis.alongi@gmail.com

Characteristics of the Fault Damage Zone From High-Resolution Seismic Imaging Along the Palos Verdes Fault, California

Travis Alongi[1,2] [iD], **Emily E. Brodsky**[1] [iD], **Jared Kluesner**[3] [iD], **and Daniel Brothers**[3] [iD]

[1]University of California, Santa Cruz, Santa Cruz, CA, USA, [2]United States Geological Survey, Moffett Field, CA, USA, [3]United States Geological Survey, Santa Cruz, CA, USA

Abstract The distribution and intensity of fault damage zones provides insight into fault activity and its relationship to fluid flow in the crust. Presently, measures of the in-situ distribution of fault damage remain limited and along-strike studies are rare. This study focuses on an offshore section Palos Verdes Fault damage zone that spans 28 km, near Los Angeles, California. To investigate the previously unresolved shallow (∼400 m below the seafloor) fault damage zone we use densely spaced (∼500 m line separation) newly collected sparker multichannel seismic lines and sub-bottom profiles. The combination of high-resolution acquisition methods and specialized seismic processing workflows provide improved imaging of shallow faulting. We apply a multi-trace similarity technique to identify discontinuities in the seismic data that may be attributed to faults and fractures. This fault detection approach reveals diverse fault damage patterns on adjacent seismic profiles. However, a discernible damage zone pattern emerges by stacking multiple damage detection profiles along strike. We find that peak damage identified in this way corresponds to the active main fault strand, confirmed in this study, and thus the technique may be useful for identifying active fault strands elsewhere. Additionally, we observe that the variable width of the damage zone along strike is controlled by fault obliquity. Furthermore, our observations reveal a correlation between fault damage and seafloor fluid seeps visible in the water column, suggesting that damage plays a role in controlling fluid flow around the fault.

Plain Language Summary The area surrounding a fault has many smaller secondary faults that make up the fault damage zone. The amount of secondary faults, or damage, holds valuable information about how faults develop and change over geologic time, which is crucial for understanding earthquakes. In this study, we use shipboard sound sources to generate around 100 images that represent the layers of rock beneath the seafloor, along 30 km along the fault's length. By analyzing features within these images, we identify and detect faults along with their accompanying damage zone. We find that shallow subsurface damage is an effective way to distinguish faults that are active from those that are inactive. We also observe that cumulative fault offset controls the approximate width of the damage zone and variation of damage along the length of the fault is related to fault bends. Additionally, our findings reveal that fluids are released from the seafloor where the fault zone is most damaged. This supports the idea that fault damage zones function as fluid pathways around faults.

1. Introduction

The distribution and intensity of fault damage zones provide valuable insights into the behavior and response of the Earth's crust to earthquakes. These fault damage zones are characterized by increased faulting, fracturing, and deformation around a fault's principal slip surface, and has been documented in numerous field and geophysical studies (e.g., Caine et al., 1996; F. M. Chester & Logan, 1986; Choi et al., 2016; Rodriguez Padilla et al., 2022; Scott et al., 2018). Studies have revealed that fault damage zones are most pronounced and observable in the uppermost kilometers of the Earth's crust (Alaei & Torabi, 2017; Alongi et al., 2022; Atterholt et al., 2022; Ben-Zion et al., 2003; Cochran et al., 2009; Li et al., 2004, 2016; Liao et al., 2019, 2020; Ma et al., 2019; Qiu et al., 2021; Thurber et al., 1997; White et al., 2021; Yang et al., 2011, 2014). Observations of fault damage are typically at depths shallower than where earthquakes nucleate, however, these zones undergo inelastic processes during coseismic rupture that alter the bulk rock properties. These changes impact near-field seismic hazards, potentially amplifying ground motions during future earthquakes and affecting the distribution of seismic energy (Kurzon et al., 2014; Spudich & Olsen, 2001; Wu et al., 2009).

Furthermore, fault damage zones are essential to understanding fundamental earthquake physics for the following reasons. They form a vital energy sink in the earthquake energy budget (Abercrombie & Rice, 2005; J. S. Chester et al., 2005; Kanamori & Brodsky, 2004; Ke et al., 2022; Martel & Pollard, 1989; Wong, 1982). Another aspect is the impact of fault damage zone rheology on dynamic earthquake rupture. The properties of fault damage zones, such as their strength and frictional behavior, can influence the propagation and evolution of earthquake ruptures (Dunham et al., 2011; Kame et al., 2003). The heterogeneity of the fault damage zone can affect rupture behavior, the seismic cycle, and seismic wave propagation (Ben-Zion and Sammis, 2010; Huang et al., 2014; Thakur et al., 2020). Additionally, fault damage zones in low porosity rock exhibit high permeability and play a crucial role in fluid flow around faults (Caine et al., 1996). Fluids stored within fault damage zones affect stress conditions and can potentially control nucleation and slip behavior (Bense et al., 2013; Guo et al., 2021; Hubbert & Rubey, 1959).

Despite the importance of the fault damage zone and associated studies, numerous key questions remain unanswered. For example, the relationship between the fault damage zone and current fault activity is unclear. It is possible that the amount of damage around the fault could be a proxy for fault activity. This notion arises from the idea that repeated slip events on the fault cause predictable patterns of rock damage. If this were correct, then the characteristics of the damage zone could be used to infer the total offset given a thorough understanding of fault history, unit age, and slip rate. On the other hand, it is equally plausible that accumulated damage may reflect geological history rather than present-day fault behavior. Resolving which of these scenarios is true is vital for interpreting the geologic record and assessing the potential to interpret characteristics of the fault damage zone to indicate fault activity.

Another subject of ongoing debate is the lateral extent of the fault damage zone. Field studies commonly observe a fault damage zone that is 10–100s of meters wide (Berg & Skar, 2005; F. M. Chester & Logan, 1986; Choi et al., 2016; Shipton & Cowie, 2001). Conversely, geophysical indicators of fault damage find damage zones wider by an order of magnitude. This has been observed in various studies including fault zone trapped waves (e.g., Ben-Zion et al., 2003; Li et al., 1997, 2004, 2016; Yang et al., 2014), low-velocity zones (e.g., Atterholt et al., 2022; Cochran et al., 2009; Qiu et al., 2021; Thurber et al., 1997; White et al., 2021; Yang et al., 2011), geodetic studies (e.g., Fialko, 2002; Fialko, 2004; Materna & Bürgmann, 2016; Xu et al., 2023), and controlled source seismic reflection studies (Alaei & Torabi, 2017; Alongi et al., 2022; Liao et al., 2019, 2020; Ma et al., 2019). Understanding the factors that control the disparity in results across methods is crucial for a unified depiction of the fault damage zone.

While the effects of bends along strike-slip faults on surface topography have been studied, their impact on the fault damage zone at depth remains unexplored. The impact of fault obliquity expressed as uplift and crustal shortening caused by restraining bends, or as subsidence induced by releasing bends, have been widely investigated (Aydin & Nur, 1982; DeLong et al., 2010; Dooley & McClay, 1997; Mann, 2007; McClay & Bonora, 2001; Segall & Pollard, 1980). Analog models provide valuable insights, demonstrating that transpressional restraining and transtensional releasing bends generate more faults and wider zones of faulting and deformation than simple linear faults (Naylor et al., 1986). Transtensional settings tend to facilitate simpler fault structures with less folding (Dooley & Schreurs, 2012), and thus a narrower fault damage zone. Observationally, the connection between surficial fault geometry and the width or complexity of fault zones has been hinted at in surface rupture maps following large intraplate earthquakes (Aydin & Du, 1995; Teran et al., 2015) and recent studies using optical image correlation techniques have also indicated an increase in strain and surface cracking at fault bends (Milliner et al., 2021; Scott et al., 2018). However, it remains to be demonstrated how fault geometry might influence the distribution of faults and damage at greater depths.

Another critical issue involves understanding how the fault damage zone responds to accumulated fault offset. Existing research has shown that the width of the fault damage zone tends to increase for faults with greater displacement (Faulkner et al., 2011; Savage & Brodsky, 2011; Torabi & Berg, 2011; Torabi et al., 2020). However, cumulative displacement can vary along a single fault. Do changes in total offset along a fault result in a variability of the fault damage zone?

Lastly, the link between damage zones and hydrological features needs to be clarified, particularly in the marine environments. While multiple studies have proposed that fluids generated at depth are structurally controlled and guided by faults to seep at the seafloor, direct in-situ subsurface data establishing a conclusive link between faults damage zones and seeps is often lacking (Kluesner & Brothers, 2016; Kluesner et al., 2013; Prouty et al., 2020;

Rudebusch et al., 2023; Tréhu et al., 1999). Therefore, connecting measurements taken at the seafloor with the extent and patterns of damage at depth is essential for extrapolating insights from data-rich bathymetry and water column measurements to less abundant Multichannel Seismic (MCS) reflection data.

To address the knowledge gaps outlined above, the present study focuses on the offshore portion of Palos Verdes Fault (PVF) in southern California and utilizes newly collected 2D high-resolution MCS and chirp sub-bottom profiles. The seismic survey design, acquisition equipment, and seismic processing techniques provide an opportunity to investigate fault damage at a mesoscale (~3 m horizontal and vertical resolution, see Text S1 in Supporting Information S1). This approach enables mapping the fault damage zone in the context of activity, outcrop versus average damage behavior, obliquity, cumulative offset, and fault zone hydrogeology, supplying new insight into this complex system at an unprecedented scale.

In this study, we show that automated fault detection is an effective technique that accurately identifies faults within high-resolution MCS data sets. The fault detections localized around the active main fault strand, even in the presence of a well-documented anastomosing fault network, demonstrating the reliability and applicability of the automated fault detection approach in capturing the actual fault location. The study establishes relationships between the fault damage zone, obliquity of the active main fault trace, and displacement. Furthermore, the study employs fault damage and fluid seep proxies to explore the role of tectonic history in controlling fluid mobility around the fault zone.

2. Tectonic Setting and Data

2.1. The Palos Verdes Fault and Tectonic Context

The PVF is approximately 100 km in length and has a northwest-southeast strike (Figure 1). The fault is both onshore and offshore in southern California within the Inner Continental Borderland tectonic province, and it accommodates a portion of the dextral shear between the Pacific and North American Plates (Figure 1). Slip rate studies indicate that the PVF has a slip rate of 1.1–5.9 mm/year and accounts for a significant percentage of total right lateral motion distributed amongst faults within the Continental Borderland (6–8 mm/year) (Brankman & Shaw, 2009; Brothers et al., 2015; McNeilan et al., 1996; Platt & Becker, 2010; Sorlien et al., 2013; Ward & Valensise, 1994; Wolfe et al., 2022). Studies employing controlled source seismic reflection data have revealed that the fault is near vertical in the sedimentary rock above the basement, which occurs at a depth of approximately 2 km (Alongi et al., 2022; Brankman & Shaw, 2009; Brothers et al., 2015; Fisher et al., 2004; Sorlien et al., 2013).

Over the past 25 million years, the crust surrounding the PVF has experienced various stress states and stages of faulting in response to the plate boundary's evolution. Before the Miocene (~25 Ma), the margin served as a convergent boundary between the Farallon and the North American Plates. In the early Miocene (~23 Ma), the plate boundary underwent reorganization, transitioning into a transform system (Crouch & Suppe, 1993). Later in the Miocene, oblique extension, rifting, and normal faults led to the development of basins in the Inner Continental Borderlands, as evident by fault-ward thickening of Miocene units east of the fault in seismic reflection data (Alongi et al., 2022; Brankman & Shaw, 2009; Fisher et al., 2004). During the early Pliocene (~6 Ma), the plate boundary stepped inland, forming the San Andreas Fault "Big Bend," and the Inner Continental Borderlands faults underwent a transition from transtensional to transpressional systems (Wright, 1991; Yeats & Beall, 1991). This led to an uplift west of the PVF, juxtaposing older rock on the west and younger rock east of the fault (Ward & Valensise, 1994) and is discussed in further detail in Section 4.2.

2.2. Data

Previous studies investigating the offshore portions of the PVF have used various controlled source seismic reflection data sets to map the fault (Alongi et al., 2022; Brothers et al., 2015; Rigor, 2003; Walton, Brothers, et al., 2020; Walton, Papesh, et al., 2020; Wolfe et al., 2022). However, data acquisition, survey design, and processing limitations have hindered the identification of secondary faults that comprise the fault damage zone at shallow depths (less than 400 m below the seafloor). As a result, there is a lack of understanding regarding the extension of the fault damage zones to the seafloor, their relationship with bathymetric features, and their influence on seafloor fluid flow.
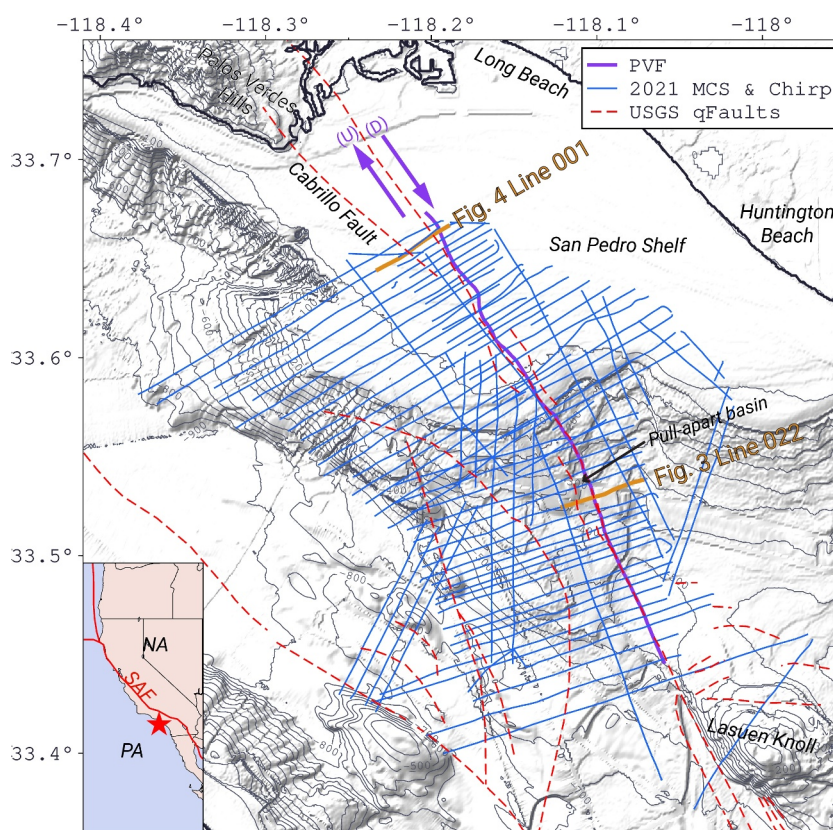
Figure 1. Map of the study area, the Inner Continental Borderland and San Pedro Shelf, in southern California. The inset map shows western North America with the red star indicating the study area offshore southern California; NA, North American Plate; PA, Pacific Plate; SAF, San Andreas Fault. Main map displays the location of mapped fault traces, with dashed red lines representing the United States Geological Survey's Offshore Quaternary faults (Walton, Brothers, et al., 2020; Walton, Papesh, et al., 2020). The solid purple line depicts the mapped location of the main active Palos Verdes Fault (PVF) strand identified in this study. The blue lines indicate the track line locations of coincident multichannel seismic (MCS) and sparker sub-bottom (Chirp) profiles used in the study (Alongi et al., 2024). Yellow lines represent the location of cross-sectional profiles shown in detail in other figures.

In May of 2021 the United States Geological Survey (USGS) led a 9-day survey aboard the Research vessel Robert Gordon Sproul to acquire high-resolution MCS using a SIG 50-tip mini sparker sound-source and EdgeTech 2300 0.5–16 kHz (chirp) sub-bottom profiles. Ninety-seven coincident MCS and chirp track lines amounting to 975 km were acquired along the San Pedro shelf and slope (Figure 1 and Figure S1 in Supporting Information S1). Open access to the processed MCS and chirp data sets are available through the USGS National Archive of Marine Seismic Surveys (Alongi et al., 2024; Triezenberg et al., 2016).

The processed MCS data have a peak frequency range between 100 and 300 Hz (Figure S2 in Supporting Information S1) and were recorded with a ~120 m Geometrics GeoEel 40-channel streamer featuring group spacings of 3.125 m and a sampling rate of 0.25 ms. The survey was conducted at a vessel speed of ~4 kts, with the streamer depth maintained at ~2 m below the sea surface using Geospace Navigator birds.

For precise measurements of the shallow expression of the fault and its associated damage zone, most of the track lines (51 out of 97) were oriented perpendicular to the PVF strike, spaced at ~500 m intervals (Figure 1 and Figure S1 in Supporting Information S1). This approach was designed to assess the fault and associated damage zone over 30 km. The newly collected high-resolution MCS data provides imagery with sufficient signal quality down to about 400 ms two-way travel time (TWT) below the seafloor reflector.

To increase sampling of the fault trace between survey tracklines we use seafloor bathymetry. We identify geomorphic features in the seafloor bathymetry such as fault related seafloor scarps and pull apart depocenters (Brothers et al., 2015, 2020; Walton, Brothers, et al., 2020; Walton, Papesh, et al., 2020). These faults related
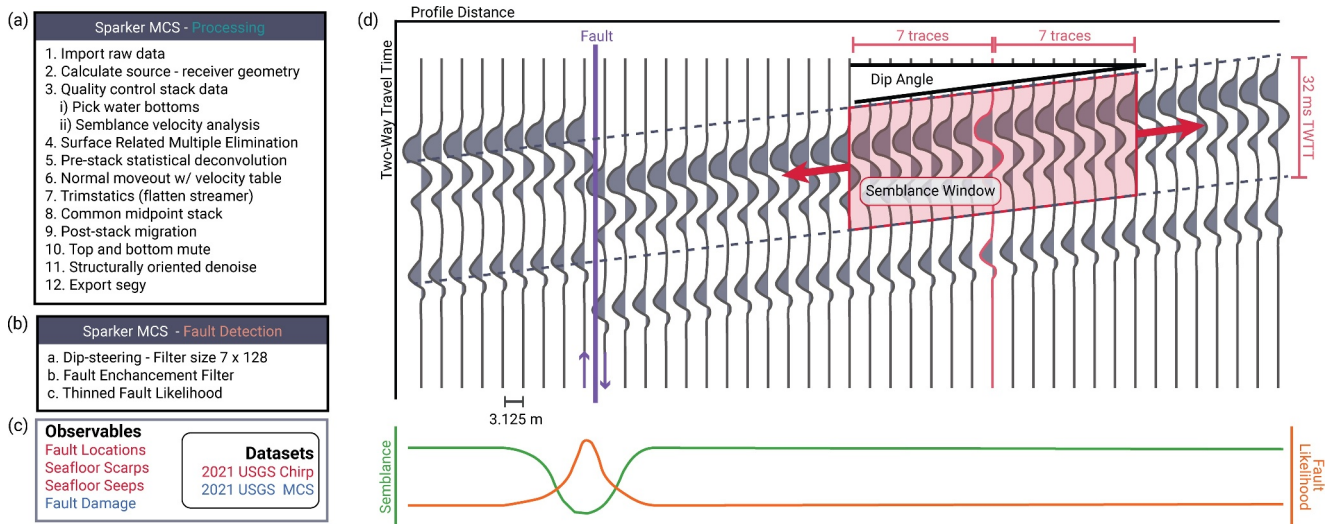
Figure 2. Schematic workflow diagram illustrating the fault detection process. (a) Processing steps for the newly collected multichannel seismic data. (b) Explanation of the fault detection workflows performed on the processed data. (c) Linking the observables and the data sets used in the study, color coded accordingly. (d) Cartoon view of semblance and fault likelihood calculation on a dipping reflector with a faulting discontinuity (highlighted by the purple line, left side up). The dip-steered semblance window follows the dip of the reflector over a moving window of 7 lateral traces and 128 samples or 32 ms two-way travel time. The green curve schematically shows semblance value of the profile tracking the dashed gray lines. The orange curve depicts the equivalent fault likelihood value as a function of profile distance, and high fault likelihood at the discontinuity.

features are observable in existing high-resolution multibeam bathymetry data (Figures S3 and S4 in Supporting Information S1) (Dartnell & Gardner, 2009; Gardner et al., 1999).

3. Data Analysis

3.1. Multichannel Seismic Processing

The newly collected MCS and chirp data were processed using Shearwater Reveal seismic software package (Reveal, 2022). The goal of the processing was to maximize horizontal and vertical resolution, minimize the impact of source and receiver ghosts, and mitigate the impact of sea surface multiples. The seismic processing steps are outlined in Figure 2, and further details can be found in Text S2 in Supporting Information S1.

The initial steps involved importing the raw field data files and calculating the source and receiver geometry using shipboard Global Navigation Satellite Systems. The seismic data collected in shallow water were affected by water column multiples, which can overprint and limit the interpretation of reflection data at depth (Dondurur, 2018). To remove these multiples, we used a modern surface-related multiple elimination workflow that mathematically predicts multiples by autoconvolution and then removes them through adaptive subtraction (Verschuur et al., 1992).

We estimated the source signature and performed pre-stack deconvolution to improve vertical resolution and reduce source ghosts and bubble-pulse (Kluesner et al., 2019; Sheriff & Geldart, 1995). Next, a critical step in high-resolution MCS data processing involves addressing along-streamer variations in receiver depths (Kluesner et al., 2019); without this step, destructive interference of high-frequency energy occurs during stacking and reduces the vertical resolution. This streamer geometry issue was addressed by applying pre-stack time shift static adjustments calculated from the cross-correlation of the windowed seafloor reflection on shot gathers. We also determined the subsurface velocity structure using semblance-based velocity analysis workflows and then applied them to normal move-out correction on common midpoint (CMP) gathers. The resulting CMP gathers were stacked to increase signal-to-noise and further suppress seafloor multiples (Yilmaz, 2001).

In order to account for wave propagation effects and more accurately image the subsurface, and move reflected energy to its proper location, migration was done in the frequency domain using a phase shift migration method (Gazdag, 1978). We migrated the post-stack data at 1,400 m/s, muting data above the seafloor and 1,200 ms TWT
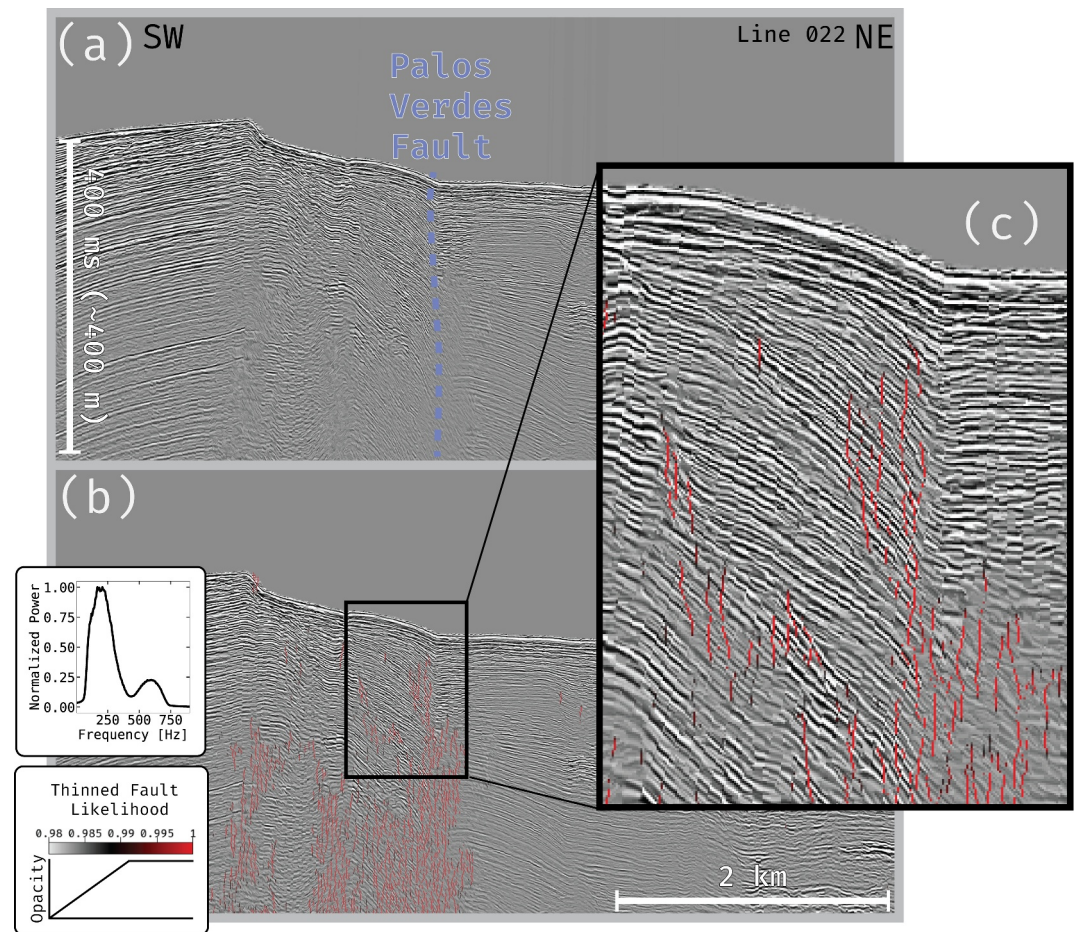
Figure 3. (a, b) A comparison of the preprocessed multichannel seismic (MCS) profile and with the thinned fault likelihood (TFL) attribute results overlain for line 022, as indicated in Figure 1. The view angle is from the southeast looking down the strike of the main active strand of the Palos Verdes Fault (PVF) (shown in purple), which is identifiable by offset reflectors, folding, and near fault deformation features. The dimensions for the figures are indicated by the white bars. (a) Presents the processed dip-steered diffusion filtered results for comparison with transparent-to-red overlay of thresholded TFL in (b). The TFL attribute is truncated to highlight high fault likelihoods (TFL > 0.98) which is consistently used throughout the study and represent high fault likelihood or dissimilarity in seismic data. (c) Provides a zoomed-in view of the fault detections around the PVF main active fault strand. Insets in the lower left display the frequency spectra of the MCS data used (top) and the color bar and transparency ramp for the TFL attribute (bottom).

below the seafloor. Finally, we removed noise introduced in the deconvolution step by applying a structurally oriented denoising workflow to depths less than 400 ms TWT below the seafloor (Hale, 2009).

3.2. Mapping the Active Main Fault Strand

To accurately map the main, or most recently active, strand of the PVF and establish it as a reference for measuring fault damage, we utilize multiple data sets, including MCS and chirp sub-bottom profiles along with high-resolution multibeam bathymetry. Our initial effort to map the fault involved strike perpendicular MCS profiles and interpreting various seismic faulting indicators such as reflector offsets, truncations, and amplitude reductions (see Figure 3). This allowed us to map the fault from the seafloor to a depth of 400 ms TWT below the seafloor, providing insight into its subsurface geometry. We observed that the fault is steeply dipping within this depth range which is consistent with previous studies (Alongi et al., 2022; Brankman & Shaw, 2009; Brothers et al., 2015; Fisher et al., 2004; Wolfe et al., 2022; Wright, 1991).

In addition to MCS data, the chirp sub-bottom profiles were important in our study, particularly in examining the upper 25 ms TWT of the fault zone and helping to identify the fault strand with the most recent surface breaking
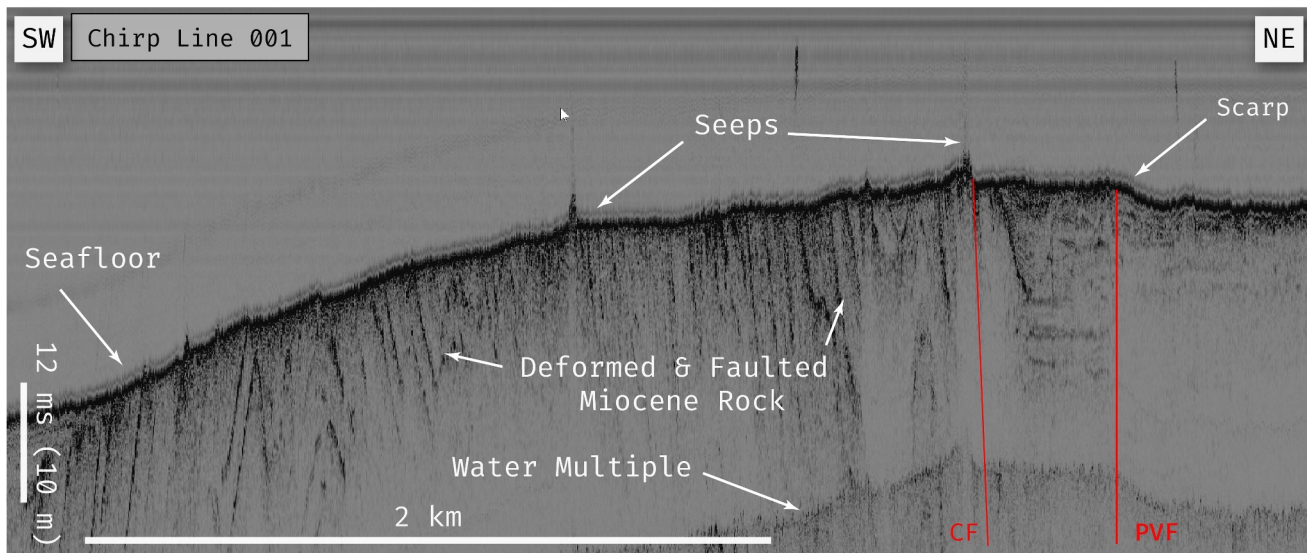
Figure 4. Chirp sub-bottom profile example for line 001, as indicated in Figure 1. The white bars indicate the length and depth with extreme vertical exaggeration of the profile to highlight the fault scarp and fluid seeps. The Palos Verdes Fault (PVF) and Cabrillo Fault (CF) are represented by the red vertical lines, marked by a sharp boundary between horizontally continuous Quaternary sediments to the northeast and deformed Miocene lithologies to the southwest. Along the shelf, all profiles crossing the fault exhibit a notable scarp at the fault location that helps determine activity. In this example, two actively flowing seafloor seeps are visible, identified by reflections in the water column created by fluid of different densities.

rupture. These profiles not only revealed offset reflections but also unveiled seafloor offsets to provide additional evidence of recent fault activity (see Figure 4). The chirp profiles reveal a fault-related scarp, with the west side of the fault elevated by as much as 3 m (refer to Figure 4 and Figure S4 in Supporting Information S1).

The scarp produced by fault offsets observed in the chirp sub-bottom profiles was also evident in the high-resolution bathymetry data (Figure S3 in Supporting Information S1). Once we had mapped the fault using the combined MCS and chirp profiles, we could trace the fault in finer detail by following geomorphic features on the seafloor. This mapping, conducted at 50-m intervals, provided us with the opportunity to evaluate the potential impact of fault bends or variations in obliquity on the pattern of fault damage. In this context, we define the reference fault strike as 156°, which is the statistical mode of the fault azimuths (see Figure S5 in Supporting Information S1) along this section. The obliquity, denoted as α, is calculated as the reference strike minus the local azimuth (Figure 5). Consequently, azimuths greater than the reference (oriented more north-south or clockwise rotation) have a negative obliquity, signifying right stepping releasing or transtensional bends. Conversely, positive obliquities are counter-clockwise rotations and are more east-west of the reference, indicating left stepping compressional or transpressional bends.

3.3. Fault Detection

We present a data-driven approach for fault detection in 2-D high-resolution MCS lines, illustrated in Figure 2. Fault detection workflows were calculated in dGB OpendTect seismic software (OpendTect, 2022). This approach utilizes the thinned fault likelihood (TFL) attribute, calculated using structurally oriented semblance over a moving space-time window (Hale, 2013). The first step is to calculate the fault likelihood attribute that is derived from semblance, which measure multi-trace similarity to infer the lateral continuity of seismic reflectors (Marfurt et al., 1998). Using a structurally oriented semblance window of 7 traces and 32 ms TWT, following the methodology in Hale (2013) fault likelihood is equal to one minus the eighth power of semblance. The resulting fault likelihood values range from 0 to 1, where 0 is low fault likelihood and 1 is high fault likelihood.

In this approach, high semblance values indicate lateral continuity of horizons or reflectors, resulting in low fault likelihood values (Figure 2d). Conversely, low semblance values indicate reflector discontinuities, leading to high fault likelihood values. This fault likelihood image is then thinned by preserving local maxima in fault likelihood. These thinned results are then connected to adjacent thinned samples over apparent dips of 75°–89°, assuming a
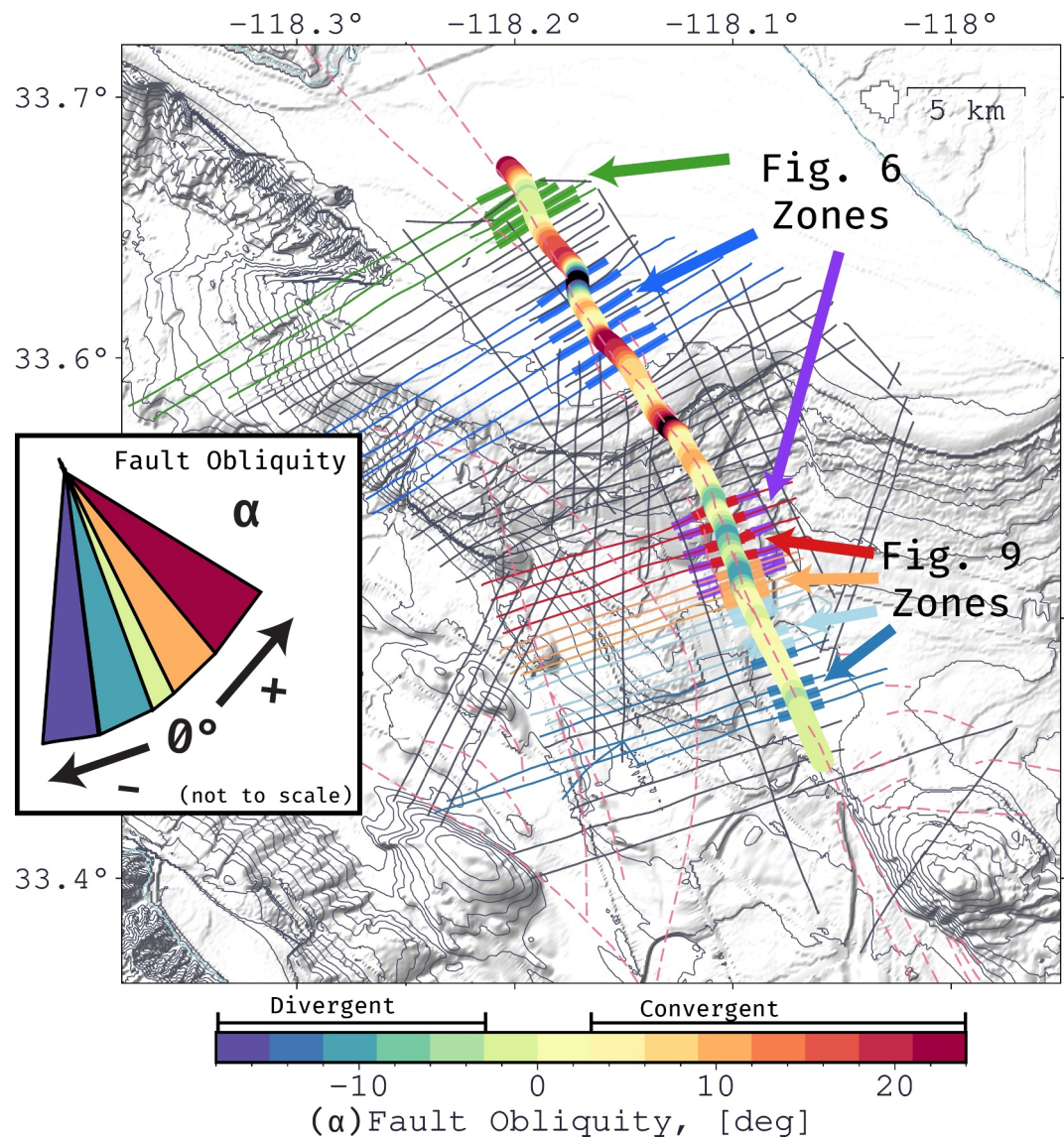
Figure 5. Illustration of the variation in obliquity along the mapped Palos Verdes Fault. The colormap transitions from purple to red, representing the relative obliquity of the fault. Green hues indicate azimuths aligned with the reference strike (156°), see Section 3.2. Cooler colors (blue and purple) indicate releasing bends and warmer colors (orange and red) are restraining bends. The inset cartoon helps visualize fault obliquity (not to scale). The green, blue, and purple lines depict the location of profiles referenced in Figure 6. The red, orange, light blue, and dark blue lines indicate the location of profiles utilized in Figure 9. The thicker portion of the colored profiles is the lateral widths use in the stacking of profiles in Figures 6 and 9.

velocity of 2,000 m/s, which represents an average local seismic velocity of the sedimentary rock at these depths (seafloor—400 ms TWT) determined from geophysical sonic well logs (Alongi et al., 2022).

Prior to calculating TFL, we pre-processed the data to enhance the lateral continuity of reflections and reduce noise we used a dip-steered fault enhancement filter. This method applies different filters based on nearby reflector dips, aiming to reduce random noise while preserving the integrity of sharp discontinuities of the fault (Chopra & Marfurt, 2008; Tingdahl & De Rooij, 2005). Specifically, a dip-steered median filter is used in areas where reflectors have shallow to moderate dips, while a dip-steered diffusion filter is applied in regions with steep dips. Figure 3 and Figure S6 in Supporting Information S1 displays the result of the fault enhancement filter and the thresholded TFL detections, which will be explored in greater detail in the next section.

3.4. Metric for Studying Fault Damage

This study investigates the spatial variation of faulting and fracturing in the damage zone related to characteristics of the active main fault strand. To achieve this, we analyze seismic lines that are approximately perpendicular to the fault's strike. This allows us to quantify fault damage as a function of distance from the fault, along approximately 25 km of the length of the PVF. By selecting the highest faulting probabilities from TFL and setting a threshold at >0.98, we focus on fault detections that a human interpreter would likely identify (Alcalde et al., 2017; Iacopini et al., 2016; Figure 3). We find that this threshold also corresponds to an approximate inflection point in the histogram of the TFL data results (Figure S7 in Supporting Information S1). Other thresholds were tested but had minimal differences and would not affect the interpretations (Figure S8 in Supporting Information S1).

Our analysis focused on the depth range extending from the seafloor to 400 ms TWT below (∼400 m assuming 2 km/s seismic velocity). This interval was chosen because it provides good signal-to-noise ratio in the data. We use the seafloor, mapped during data processing, to define the depth and extent of our investigation. To quantify fault damage, we count the number of samples in the trace that exceeded 0.98 TFL, which we refer to as thresholded counts throughout the study. Where each seismic trace is a 1D depth sampling of the TFL fault detections and consists of 1,600 samples (resulting from 400 ms TWT depth span at a 0.25 ms MCS sampling rate).

In order to examine how fault damage varies with distance from the fault, we measure the distance from each trace or sample to the location of the active fault (Section 3.2). Given the variability in the results of fault damage (thresholded counts) with distance from the fault, we adopt a stacking approach to explore the average properties of the fault damage (Figure 6). To create these stacked profiles, we regularize the geometry of the track lines by resample the damage curves at uniform 3-m distance increments by interpolation. This allows us to median stack the 2-D curves and effectively collapse the fault detection results along strike. These stacked results provide insights into the emergent characteristics of fault damage over the scale of the seismic survey (∼30 km). Differences in observed stacked damage curves are discussed in Sections 4.2 & 4.3.

3.5. Seafloor Fluid Seeps and Fault Damage

The conventional depiction of fault zone structure in low porosity rock often portrays the tabular area around the principal slipping surface as more permeable than the surrounding host rock (Bense et al., 2013; Caine et al., 1996). This permeability contrast has been recognized as a significant factor in controlling fluid flow around faults (Caine et al., 1996; Guo et al., 2021). In this study we map fluid seeps along the fault through observations of acoustic flares detected in the water column on chirp sub-bottom profiles (e.g., Figure 4 and Figure S9 in Supporting Information S1). These disturbances result from impedance differences caused by density variations between gaseous seeping fluid and ambient seawater (Suess, 2020). All chirp sub-bottom profiles were examined and 27 seeps were mapped. It is important to emphasize that the observed seeps represent a snapshot in time, portraying their activity during the survey. Additionally, the seeps are identified in 2D profiles that ensonify a narrow zone within the water column and seafloor. The actual distribution of seeps is likely much more extensive than what the results depict and would require full coverage of multibeam water column data to map. We qualitatively compare the seep locations with the fault detection data, and we find that seeps tend to concentrate in areas of high likelihood of faulting, particularly in proximity to the mapped active main fault; further details will be discussed in Section 4.5.

4. Results and Discussion

Through the development of an automated fault detection workflow, detailed mapping of the active main fault strand, and identification of fluid-seeps, this study addresses several critical issues raised in the introduction about the shallow (seafloor—400 ms TWT below or roughly 400 m) fault damage zone. The fundamental questions raised are: (a) What is the relationship between the detected fault damage zone and current fault activity? (b) How robust is the observed lateral extent of damage? (c) Does fault obliquity control the variability in damage along strike? (d) Does cumulative offset explain the variability in damage along strike better or worse than obliquity? (e) What is the observable connection between hydrogeology and the fault damage zone? Each of these questions will be systematically explored in the subsequent subsections.
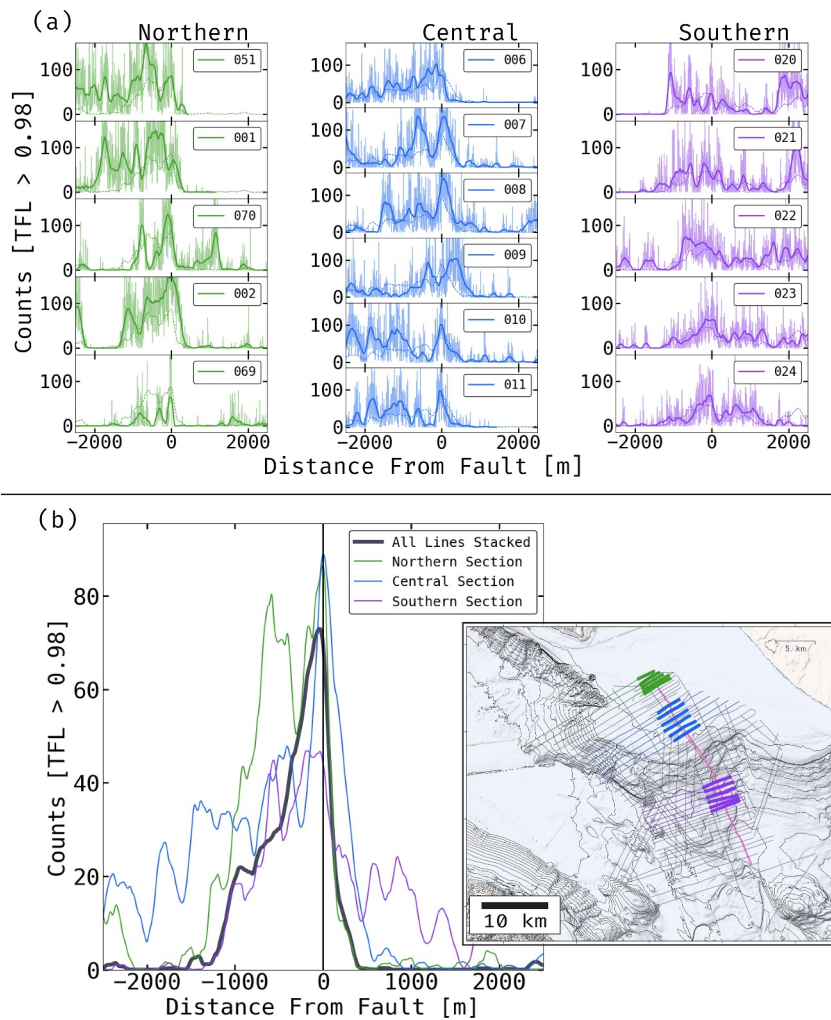
Figure 6. Visualization of the distribution of high probability (>0.98) thinned fault likelihood (TFL) detections variations with distance from the active main fault strand, calculated from the multichannel seismic data over the depth range from the seafloor to 400 ms two-way travel time below the seafloor. (a) Illustrates individual line curves for different fault sections, as indicated in the inset map in (b), and the pink line is the trace of the Palos Verdes Fault. In (a), the lines are arranged in order from north to south for their respective sections, with the line number provided in the upper right corner; see Figure S1 in Supporting Information S1 for a detailed track line map. The light-weight lines represent the number of samples in the trace (3 m sampling) that exceeded 0.98 TFL. The heavy-colored lines indicate smoothed data using a moving mean with a tapered cosine window (200 m width). (b) The median stack of each section as shown in (a). The heavy-weight dark line represents the median stack of all fault perpendicular lines. It is important to note the variability in the fault zone in individual profiles compared with the averaged values.

4.1. Damage Highlights Active Main Fault Strand

Our analysis demonstrates that stacking thresholded fault detections, derived from TFL, closely aligns with the active main fault strand of the PVF (Figure 6b). There is a notable alignment between the peak in the stacked TFL results and the location of the active main strand, confirmed in this study (Section 3.2) and agree within approximately 50 m. This observation is intriguing because the peak in fault detections occurs at the location of the active main strand even in the presence of the well documented multi-stranded PVF observed in this study and at greater depths (Alongi et al., 2022; Brankman & Shaw, 2009; Sorlien et al., 2013; Walton, Brothers, et al., 2020; Walton, Papesh, et al., 2020) (Figure 6 and Figure S10 in Supporting Information S1).

A good example of TFL's ability to identify faults is shown by the northern section of stacked profiles, represented by the green curve in Figure 6b and Figure S6a in Supporting Information S1; where there are two distinct peaks in damage detections that can be attributed to the splay in the fault zone here. One peak of fault damage aligns

with the main fault strand itself, while the other is located approximately 800 m to the west. The suggestion of a second strand from damage is consistent with faulting identifiable in chirp subbottom profiles (Figure 4 and Figure S6a in Supporting Information S1) and location of the Cabrillo Fault provided by the USGS's Offshore Quaternary Faults database (Walton, Brothers, et al., 2020; Walton, Papesh, et al., 2020) which includes a bifurcation of the fault as it extends northward (Figure 1). The eastern strand is continuous and has been confirmed to extend into Santa Monica Bay, where the western strand is not apparent beyond the Palos Verdes Peninsula (Wolfe et al., 2022). The amplitude of the peak delineating the eastern strand is greater than for the western peak, which makes sense when considering that the eastern strand is longer and has experienced more cumulative slip and thus more damage, this idea is discussed further in Section 4.4.

The correspondence between the peak in fault detections and the location of the independently mapped faults may be a two-way relationship. It suggests that peaks in fault detection may be a useful tool to aid fault mapping efforts, particularly for identifying recently active fault strands within recently deposited shallow sediments. This fault detection approach complements existing methods for fault mapping and may improve the accuracy of active fault identification, an important factor in seismic hazard assessment.

4.2. Average Fault Damage Pattern Robustness

The analysis of fault detection using high-resolution MCS data reveals a remarkable degree of variability in damage results along strike, even on closely spaced lines. However, this complexity diminishes as we stack an increasing number of fault detection curves (Figure 6). Each seismic profile and fault damage measurement represents an in-situ cross-section through the subsurface and share many characteristics with outcrops of faults in the field, albeit at 3-m resolution (for additional information on seismic resolution see Text S1 in Supporting Information S1). However, when many lines are stacked or the fault detections are averaged along strike, a smoothed pattern of fault damage emerges, as depicted in Figure 6b. These findings imply that the complexity in geologic observations of fault zones and the smoother characterizations of the damage zone often found in geophysical measurements of the damage zone may be reconciled. Stacking the damage profiles is like many geophysical measurements in that it integrates damage proxies over distance (i.e., tomography, fault zone trapped waves, geodesy) thus representing average damage complexity.

The detected damage zone becomes systematic in its behavior with additional realizations, samplings, or measures of the fault zone. The well-defined average behavior implies that these averages can be reasonably and confidently incorporated into regional scale dynamic earthquake rupture models, but should not be expected to apply to each individual outcrop.

4.3. Fault Obliquity Impacts the Fault Damage Zone

In the following two sections, we delve into two potential factors contributing to the variability in damage along strike and determine their relative importance.

First, we seek to understand how fault obliquity manifests as fault damage. To achieve this, we leverage the detailed measurements of the fault trace to calculate the fault azimuth (detailed in Section 3.2), which vary by up to 25° (See Figures 5 and 7). In this section we explore how these bends in the fault or changes in strike create zones of transpression and transtension (Mann, 2007; Sanderson & Marchini, 1984; Sylvester, 1988) that may manifest as additional fault strands and deformation patterns.

To assess the impact of obliquity of fault damage, we calculate the deviation from the reference azimuth (156°) which we define based on the statistical mode from the distribution of azimuths (Figure S5 in Supporting Information S1). This reference azimuth matches the strike of the fault in the southern portion of the survey area where there is a marked decrease in near fault folding and vertical offset across the fault which provides further clues that the reference azimuth is the preferred orientation of the fault within the local stress field. Obliquity, α, is calculated as the reference azimuth minus the azimuth defined at 50 m intervals along the fault trace. Figure 7b displays the results of the obliquity calculation as a function of distance along strike.

Next, we categorize the 40-fault perpendicular fault detection profiles into five bins based on obliquity and stack the curves following the method outlined in Section 3.4. For equitable comparison between the obliquity stacks we require an equal number of observations (damage curves) in each obliquity bin. Equal size bins are important
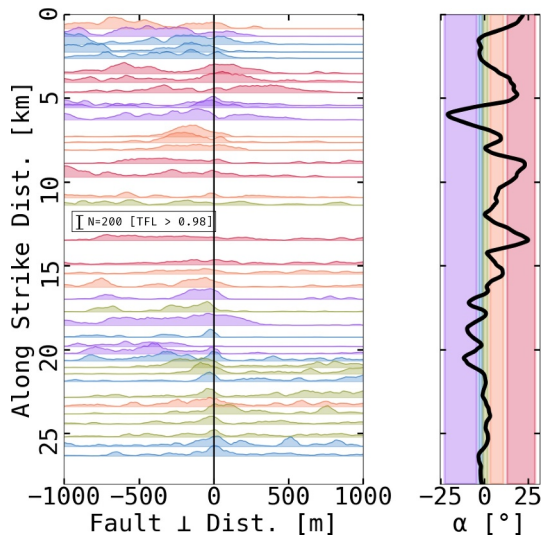
Figure 7. Illustrating the variability in the fault detections and fault obliquity with distance along strike. (Left) the curves depict the counts of thresholded Thinned Fault Likelihood calculation (TFL > 0.98) as a function of distance from the fault. For display purposes a scalebar shown at 12 km along strike showing height of 200 counts. Shading under each fault detection curve aids in visualization. Positive fault perpendicular distances are locations east of the fault and the along strike distance is measured with respect to the northwestern edge of the survey (Figure 1). (Right) illustrates obliquity, α in degrees that fluctuates along the fault's length. Positive α values are considered compressional regions, while negative α denotes extensional conditions. The obliquity bins (eight curves each) utilized for stacking the data in Figure 8 are highlighted in purple, blue, green, orange, and red accordingly, with curves contributing to the obliquity bin maintaining color consistency.
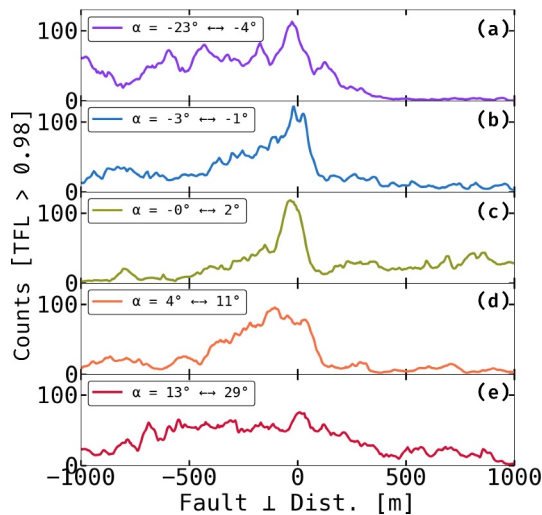

Figure 8. Fault damage data are stacked according to the obliquity of the fault. The different colors represent the obliquity (α) of the fault with respect to the reference trend, see text in Section 4.3. (a, b) The purple and blue curves represent releasing fault bends. (c) The green curve is interpreted to be well aligned with the reference orientation of the fault. (d, e) The yellow and red curves represent restraining fault bends.

because of the smoothing effect that occurs when increasing the number of curves in the stack (as discussed in Section 4.2) and could bias qualitative comparison. The stacked results are presented in Figure 8.

The stacked obliquity curves presented in Figure 8 show the relationship between the degree of obliquity and the width of the damage zone. The green curve (Figure 8c), representing a very narrow obliquity range (0°–2°), is essentially the reference azimuth and features the most localized and narrow fault damage zone or steeper flanks around the peak damage (Figure S11 in Supporting Information S1). Many of the individual curves contributing to reference azimuth range stacked results are in the southern region of the survey area, where we observe less near-fault deformation and fewer fault strands. We interpret this obliquity range to be the preferred orientation of the because the fault zone is narrow (Figure 7), and it is also the most common fault azimuth. Based on this interpretation, wider and more distributed blue and orange curves (Figures 8b and 8d, Figure S11 in Supporting Information S1) may be caused by the increased relative obliquity. We find that when obliquity increases further as in Figures 8a and 8e, we observe an even broader distribution of damage and a less identifiable "main strand" or peak in damage (Figure S6b in Supporting Information S1). The correlation between obliquity and the lateral extent of deformation is consistent with analog experiments (Dooley & Schreurs, 2012), observations of deformation along strike-slip faults (Scott et al., 2020), as well as theoretical considerations that suggest that a broader off-fault damage zone may be expected due to the rotation of the strain ellipsoid (Fossen & Tikoff, 1993; Sanderson & Marchini, 1984). We suspect that the increase in damage west of the fault in the divergent curve (Figure 8a) may be due to the superposition of basin-bounding normal faults in the pull-apart basin (Figure 1, Figures S6 and S12d in Supporting Information S1) that increase in separation to the northwest (Figure 7 along strike distances between 15 and 20 km). Thus, we conclude that obliquity is a determining factor in the variability of along strike damage.

4.4. How Cumulative Fault Displacement Relates to the Fault Damage Zone

In this section, we explore the potential relationship between cumulative displacement on the Palo Verdes Fault and fault damage. To best isolate the impact of cumulative displacement from obliquity we concentrate on the southern section of the surveyed area where the fault is relatively straight (see Figure 9 zones labeled in Figure 5).

In order to compare estimated displacement along the fault to the damage zone width we first need to determine the lateral limits or width of the damage zone. To achieve this, we measure the width by identifying the left and right edges of the stacked damage curve as the location on each side of the peak thresholded damage counts (~0 distance from fault) where the count value equals 5% of the maximum value. To determine the damage zone width, we subtract the distance between the edges. We assess the reliability of our edge determination by bootstrap resampling with replacement of the data (distance, counts pairs), following the approach outlined by Efron and Tibshirani (1994). Through 1,000 bootstrap iterations of the pairs of distances and counts and subsequent estimations of the damage curve edges (indicated as stars in Figure 9a). This analysis confirms the stability of our width metric (Figure 9c).
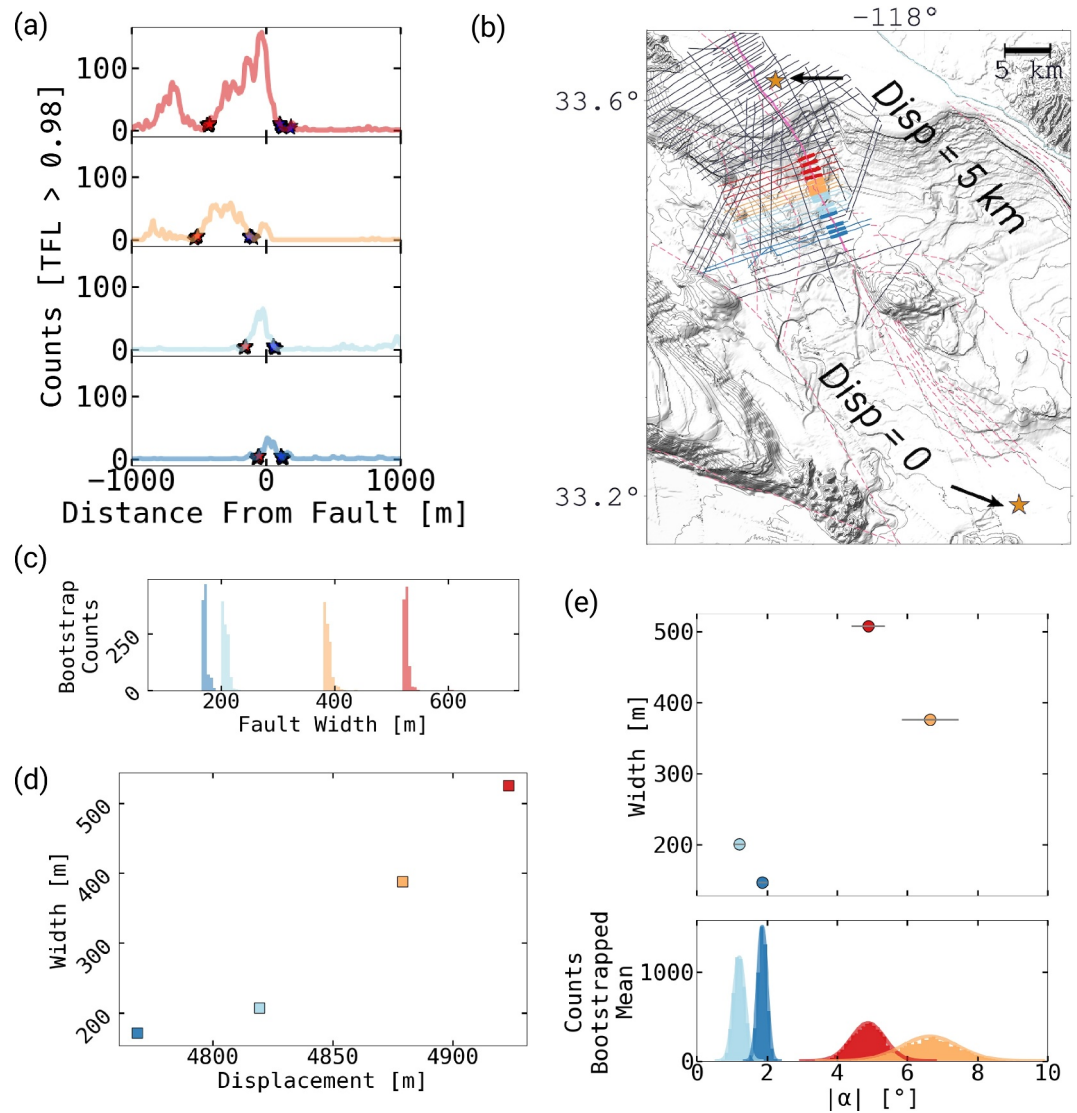
Figure 9. Shows the decrease in fault damage toward the south. Panel (a) displays the variation of stacked and thresholded thinned fault likelihood (TFL > 0.98) with distance east of the active main strand of the fault, similar to the plots shown in Figure 6. The stars on the curve represent the edges of the damage zone, defined as where the value equals 5% of the peak damage with the red and blue stars corresponding to the western and eastern edges, respectively. The locations of each stack subsection are depicted in (b) where colors remain consistent in all subplots. The curves and edges are obtained through 1,000 bootstrap iterations, and the results for the measured edge distances are presented in (c). (d) Showing fault zone width as a function of estimated displacement, details on the displacement estimation are presented in the text, Section 4.4. (e) Displaying fault zone width as a function of the absolute value of obliquity (α) described in the text, Section 3.2. The error bars represent 1 standard deviation of the bootstrapped means of obliquity for each segment and the distributions are shown below.

We then must estimate displacement, which unfortunately cannot be measured directly along-strike. We therefore use a theoretical relationship to estimate displacement as a function of distance from the fault tip using two key assumptions. (a) Fault slip converges to zero at the fault tip (Segall, 2010). (b) Slip rate has remained constant over time (Cowie et al., 2012). We estimate displacement for four subsections of the fault in the southern region of the survey (depicted in Figure 9) using the elliptical relation between displacement and the distance from the fault tip that is theoretically derived from linear elastic theory (Bürgmann et al., 1994; Pollard et al., 1987; Tada et al., 1973). Other relationships between along strike distance and displacement have been observed and are topic of continuing discussion, however, model choice does not impact our interpretation (Figure S13 in Supporting Information S1). See Text S3 in Supporting Information S1 for details on displacement estimated from distance
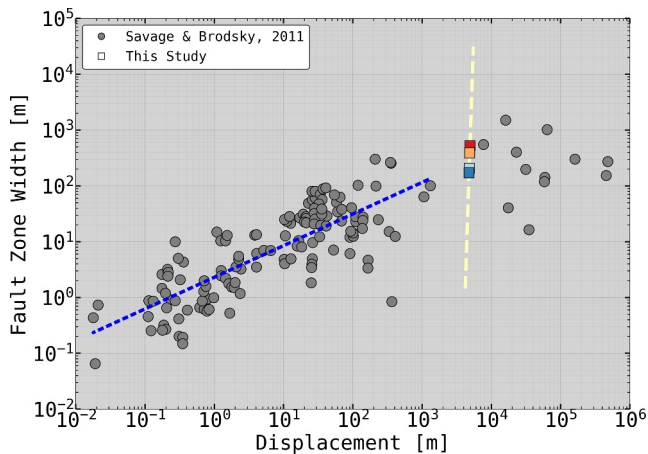
Figure 10. Comparison of the damage zone width versus displacement from this study along with previous compilation study results. The colored squares indicate widths that were estimated from bootstrapping results that were presented in Figure 9, and marker the faces are colored by distance from the end of the fault. The dotted blue line is the power law fit to the data provided in Savage & Brodsky, 2011. The dashed yellow line is the power law fit for the data in this study.

from the fault tip. Our calculation uses an estimated displacement of 5 km on the mid-shelf, based on measured offset of a Miocene sediment isopach (Brankman & Shaw, 2009). The fault tip (zero displacement) is the location where seismic reflection data no longer shows evidence of the PVF (Line WSD81-712, Triezenberg et al., 2016). These two locations are shown in Figure 9.

The analysis indicates that damage width steadily decreases to the south-east, also apparent in MCS data (Figure S11 in Supporting Information S1) along approximately 13 km of fault length (Figures 9a, 9b, and 9d). It may be tempting to attribute the decrease in damage width to scaling relationships that link damage width to cumulative slip (Alaei & Torabi, 2017; Savage & Brodsky, 2011). And, while our results are consistent with compilation studies of damage zone width and displacement (Figure 10, square points; Savage & Brodsky, 2011), there is a striking deviation from the compilation trend. The pronounced increase in the damage zone width with displacement for the four points from this study is much greater than the scaling relationship alone predicts (Figure 10). This leads us to conclude that the overall width is likely governed by fault displacement, but that the rapid increase in width to north (away from the fault tip) may be better explained by the change in obliquity shown in Figure 9e. In other words, the displacement along the fault likely sets the general width of the fault damage zone, while fault obliquity accounts for along strike variations in damage zone width.

4.5. Fault Damage Controls Fluid-Flow

Our analysis reveals a clear spatial correlation between the locations of active fluid seeps and the TFL attribute, as shown in the map in Figure 11a. This correlation (Figure 11b) suggests that the fault damage, which provides enhanced permeability (Bense et al., 2013; Caine et al., 1996; Faulkner et al., 2010), is facilitating the escape of fluids from the seafloor that we observe in the chirp sub-bottom profiles.

Interestingly, we find that seeps are predominantly observable to the west of the fault and are primarily confined to the shelf area. This indicates that faults alone are not the sole control on seafloor seepage. There is a clear asymmetry to the stacked fault damage zone trends (Figure 6b). On the shelf where the seeps are, there is a preference for damage to extend further to the west of the fault, while fault damage appears to be more localized east of the fault. We attribute this damage asymmetry to the well-documented tectonic folding and uplift occurring west of the fault (Brankman & Shaw, 2009; Sorlien et al., 2013; Ward & Valensise, 1994). This anticlinal uplift has resulted in older, more deformed/faulted rock being juxtaposed against younger, less deformed rock on opposite sides of the fault, schematically shown in Figure 12. Subsequently, the increased fault damage on the western side of the fault maybe attributed to the presence of more deformed and fractured older rocks. These more fractured rocks presumably provide pathways for focused fluid flow and may explain the pattern of seafloor seeps.

The absence of seeps to the east of the fault as well as on the slope may be due to young sediment cap may prevent vertical fluid flow in these areas. There is evidence for these trapped fluids in the MCS data which are identifiable as "bright spots" (Figure S14 in Supporting Information S1), a common gas indicator (Løseth et al., 2009). We suspect that the series of seeps observed at the eastern edge of the study area are associated with the damage zone of the Thums-Huntington Beach fault.

Overall, our findings highlight the complex interplay between faulting, permeability, and fluid flow dynamics in the study area, outlined in Figure 12. The correlation between active fluid seeps and the TFL attribute suggests that fault damage provide preferential pathways for fluid migration and escape like other seismic reflection studies conducted along the Hosgri Fault, offshore California (Kluesner & Brothers, 2016). Understanding the factors controlling fluid seepage in this region is crucial for comprehending the broader feedback between tectonics and fluid flow.
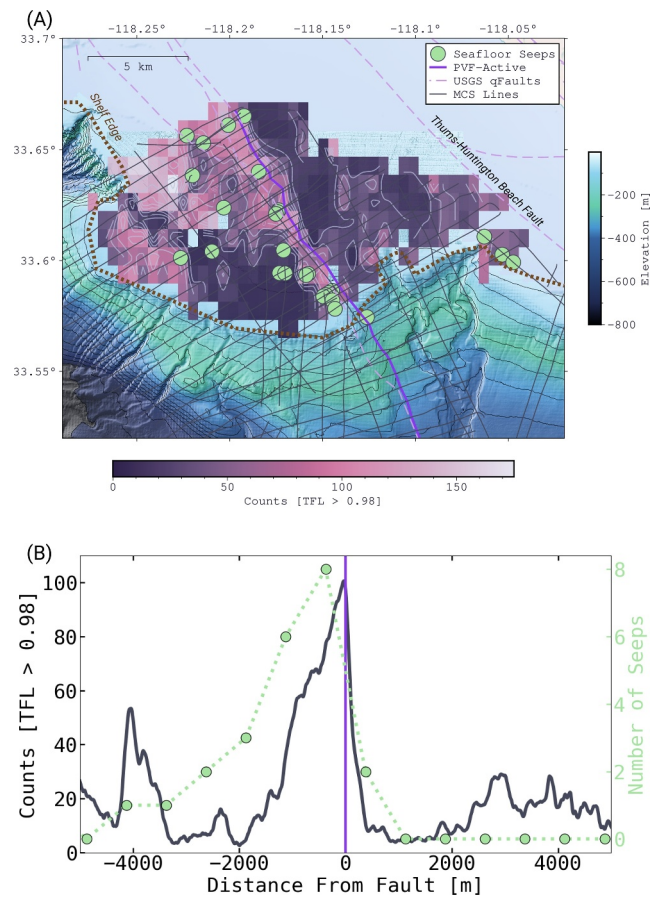
Figure 11. Comparison of the thresholded thinned fault likelihood attribute (TFL) with the locations of the manually mapped seafloor seeps depicted by light green circles. (a) The TFL color palette ranges from purple at low fault detection levels, to white representing highly faulted areas. Additionally, a contour of the TFL detections is included to assist the reader. Fault detection data is displayed for shelf regions, and the shelf break is represented by a dashed brown line. (b) Comparison of binned number of seeps and thresholded TFL detections as a function of lateral distance east of the fault.

5. Conclusions

In conclusion, our study investigates fault damage zones, fluid seeps, and their relation to the active main strand of the PVF. Using high-resolution MCS, multibeam bathymetry, and chirp sub-bottom profiles, we have identified the active main fault strand and characterized the damage distribution along the broader fault zone. We observe the highest intensity of damage occurring at the location of the mapped main active fault strand. Our findings demonstrate the effectiveness of the automated fault detection method in accurately identifying the active main fault strand within a complex fault network, thereby presenting a tool for future studies in fault mapping, analysis, and seismic hazard assessment.

We note that the fault zone is highly variable in signature and lateral extent in seismic reflection profiles; however, a consistent pattern emerges when fault detections are averaged along strike. This suggests that the smoothness of fault damage zones observed in other geophysical studies is likely a low pass filtered or smoothed depiction of the fault zone and that could be obscuring the real complexities observed in field studies.

Furthermore, we uncover a connection between the degree of damage localization and the obliquity of the fault. Our findings indicate that increasing fault obliquity, whether in restraining or releasing bends, amplifies the distributed nature of the fault damage zone. This insight into fault obliquity explains the variation in fault damage observed along the length of the fault. We think that to first order the overall width and distribution of the damage zone is likely controlled by displacement and that along strike variability is impacted by fault obliquity.
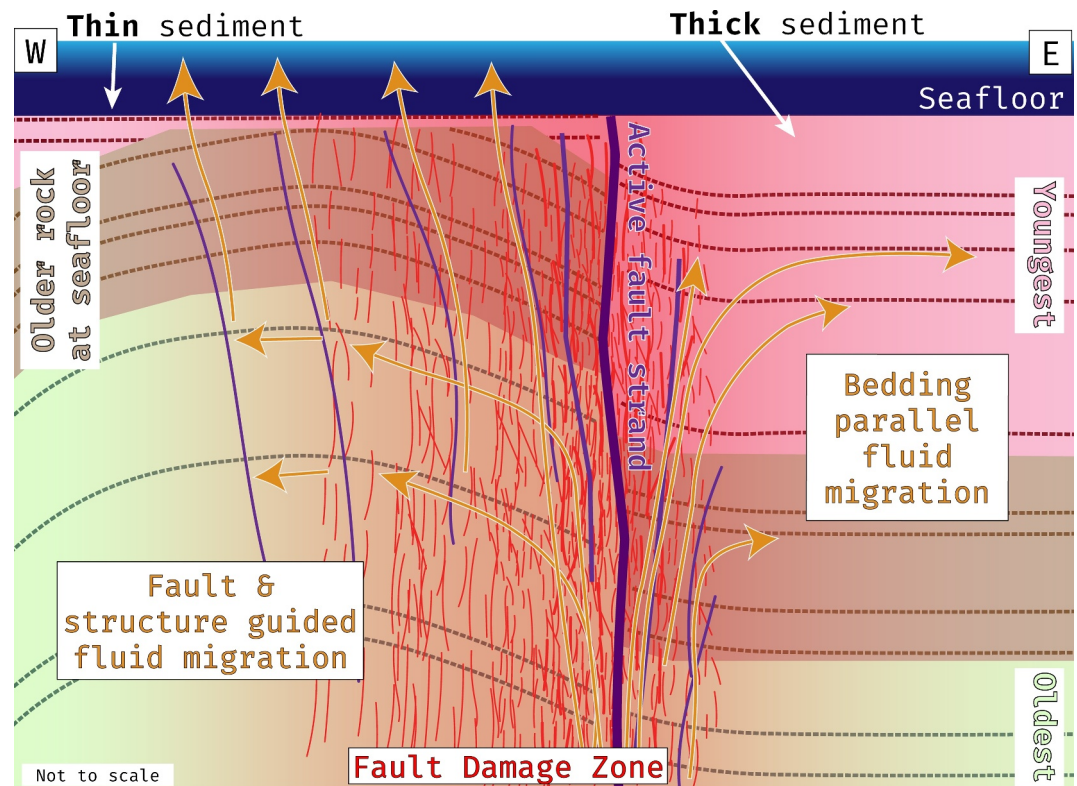
Figure 12. Schematic cross-section cartoon representing the fluid system in Section 4.5 of the text. Fluids generated at depth migrate toward the seafloor through the high permeability fault damage zone, represented by red subvertical lines. The fault damage, combined with the tectonic history of the Palos Verdes Fault region, influences the spatial distribution of fluids released at the seafloor. Long-term uplift west of the fault brings older, more damaged rock closer to the seafloor, preventing the accumulation of Quaternary sediments; this facilitates the uninhibited release of fluids. Conversely, to the east of the fault where the damage is low and a thick sediment cap exists, fluids tend to be trapped within formation beds.

By combining the fault damage analysis with observations of fluid seepage patterns, we uncover the role of tectonic history and sedimentation in controlling fluid mobility around the fault. The observed correlation between fault damage and fluid seeps provides insight into how faults within a strike-slip system govern subsurface fluid flow and expulsions at the seafloor. The absence of fluid seeps in areas with thick quaternary sediment suggests that the fluids are trapped in these layers without any clear pathways (faults/fractures) to the seafloor.

Altogether, fault zone damage as measured in shallow seismic data has proven to be a robust and useful tool to identify active faults, to determine the key factors governing inelastic deformation and to directly observe the controls on fluid migration in the crust.

Conflict of Interest

The authors declare no conflicts of interest relevant to this study.

Data Availability Statement

Data was collected and processed for the purposes of this study is available through the USGS's seismic reflection repository, National Achieve of Marine Seismic Surveys (https://walrus.wr.usgs.gov/namss/search/). The multichannel minisparker and chirp seismic reflection data for this study (2021-614-FA) is openly available at https://doi.org/10.5066/P9HCOSDF (Alongi et al., 2024). These data sets were processed using ShearWater Reveal (https://www.shearwatergeo.com/) seismic processing software, versions 4 and 5, using an academic license donated by ShearWater. Seismic interpretation and fault identification was done with academic licenses in Kingdom Suite (https://kingdom.ihs.com/) and OpendTect (https://dgbes.com/software/opendtect). Data analysis

and figures were created using python 3.11.8. Most maps were created using pygmt (Uieda et al., 2021) using Generic Mapping Tools (GMT) version 6 (Wessel et al., 2019) licensed under LGPL version 3 or later, available at https://www.genericmapping-tools.org/. Some maps were created using QGIS version 3.34 (http://www.qgis.org/).

References

Abercrombie, R. E., & Rice, J. R. (2005). Can observations of earthquake scaling constrain slip weakening? *Geophysical Journal International*, *162*(2), 406–424. https://doi.org/10.1111/j.1365-246X.2005.02579.x

Alaei, B., & Torabi, A. (2017). Seismic imaging of fault damaged zone and its scaling relation with displacement. *Interpretation*, *5*(4), SP83–SP93. https://doi.org/10.1190/INT-2016-0230.1

Alcalde, J., Bond, C. E., Johnson, G., Ellis, J. F., & Butler, R. W. H. (2017). Impact of seismic image quality on fault interpretation uncertainty. *GSA Today*. https://doi.org/10.1130/GSATG282A.1

Alongi, T., Balster-Gee, A. F., Kluesner, J. W., Snyder, G. R., Brothers, D. S., Conrad, J. E., & Marcuson, R. K. (2024). Multichannel minisparker and chirp seismic reflection data collected during USGS field activity 2021-614-FA along the Palos Verdes Fault Zone [Dataset]. *U.S. Geological Survey Data Release*. https://doi.org/10.5066/P9HCOSDF

Alongi, T., Brodsky, E. E., Kluesner, J., & Brothers, D. (2022). Using active source seismology to image the Palos Verdes Fault damage zone as a function of distance, depth, and geology. *Earth and Planetary Science Letters*, *600*, 117871. https://doi.org/10.1016/j.epsl.2022.117871

Atterholt, J., Zhan, Z., & Yang, Y. (2022). Fault zone imaging with distributed acoustic sensing: Body-to-surface wave scattering. *Journal of Geophysical Research: Solid Earth*, *127*(11), e2022JB025052. https://doi.org/10.1029/2022jb025052

Aydin, A., & Du, Y. (1995). Surface rupture at a fault bend: The 28 June 1992 Landers, California, earthquake. *Bulletin of the Seismological Society of America*, *85*(1), 111–128.

Aydin, A., & Nur, A. (1982). Evolution of pull-apart basins and their scale independence. *Tectonics*, *1*(1), 91–105. https://doi.org/10.1029/tc001i001p00091

Bense, V., Gleeson, T., Loveless, S., Bour, O., & Scibek, J. (2013). Fault zone hydrogeology. *Earth-Science Reviews*, *127*, 171–192. https://doi.org/10.1016/j.earscirev.2013.09.008

Ben-Zion, Y., Peng, Z., Okaya, D., Seeber, L., Armbruster, J. G., Ozer, N., et al. (2003). A shallow fault-zone structure illuminated by trapped waves in the Karadere-Duzce branch of the North Anatolian Fault, western Turkey. *Geophysical Journal International*, *152*(3), 699–717. https://doi.org/10.1046/j.1365-246X.2003.01870.x

Ben-Zion, Y. & Sammis, C. G. (Eds.). (2010), *Mechanics, structure and evolution of fault zones*. Birkhäuser.

Berg, S. S., & Skar, T. (2005). Controls on damage zone asymmetry of a normal fault zone: Outcrop analyses of a segment of the Moab fault, SE Utah. *Journal of Structural Geology*, *27*(10), 1803–1822. https://doi.org/10.1016/j.jsg.2005.04.012

Brankman, C. M., & Shaw, J. H. (2009). Structural geometry and slip of the Palos Verdes Fault, Southern California: Implications for earthquake hazards. *Bulletin of the Seismological Society of America*, *99*(3), 1730–1745. https://doi.org/10.1785/0120080303

Brothers, D. S., Conrad, J. E., Maier, K. L., Paull, C. K., McGann, M., & Caress, D. W. (2015). The Palos Verdes Fault offshore Southern California: Late Pleistocene to present tectonic geomorphology, seascape evolution, and slip rate estimate based on AUV and ROV surveys. *Journal of Geophysical Research: Solid Earth*, *120*(7), 4734–4758. https://doi.org/10.1002/2015JB011938

Brothers, D. S., Miller, N. C., Barrie, J. V., Haeussler, P. J., Greene, H. G., Andrews, B. D., et al. (2020). Plate boundary localization, slip-rates and rupture segmentation of the Queen Charlotte Fault based on submarine tectonic geomorphology. *Earth and Planetary Science Letters*, *530*, 115882. https://doi.org/10.1016/j.epsl.2019.115882

Bürgmann, R., Pollard, D. D., & Martel, S. J. (1994). Slip distributions on faults: Effects of stress gradients, inelastic deformation, heterogeneous host-rock stiffness, and fault interaction. *Journal of Structural Geology*, *16*(12), 1675–1690. https://doi.org/10.1016/0191-8141(94)90134-1

Caine, J. S., Evans, J. P., & Forster, C. B. (1996). Fault zone architecture and permeability structure. *Geology*, *24*(11), 1025. https://doi.org/10.1130/0091-7613(1996)024<1025:FZAAPS>2.3.CO;2

Chester, F. M., & Logan, J. M. (1986). Implications for mechanical properties of brittle faults from observations of the Punchbowl fault zone, California. *Pure and Applied Geophysics*, *124*(1–2), 79–106. https://doi.org/10.1007/BF00875720

Chester, J. S., Chester, F. M., & Kronenberg, A. K. (2005). Fracture surface energy of the Punchbowl fault, San Andreas system. *Nature*, *437*(7055), 133–136. https://doi.org/10.1038/nature03942

Choi, J.-H., Edwards, P., Ko, K., & Kim, Y.-S. (2016). Definition and classification of fault damage zones: A review and a new methodological approach. *Earth-Science Reviews*, *152*, 70–87. https://doi.org/10.1016/j.earscirev.2015.11.006

Chopra, S., & Marfurt, K. (2008). Gleaning meaningful information from seismic attributes. *First Break*, *26*(9), 11. https://doi.org/10.3997/1365-2397.2008012

Cochran, E. S., Li, Y.-G., Shearer, P. M., Barbot, S., Fialko, Y., & Vidale, J. E. (2009). Seismic and geodetic evidence for extensive, long-lived fault damage zones. *Geology*, *37*(4), 315–318. https://doi.org/10.1130/G25306A.1

Cowie, P. A., Roberts, G. P., Bull, J. M., & Visini, F. (2012). Relationships between fault geometry, slip rate variability and earthquake recurrence in extensional settings. *Geophysical Journal International*, *189*(1), 143–160. https://doi.org/10.1111/j.1365-246x.2012.05378.x

Crouch, J. K., & Suppe, J. (1993). Late Cenozoic tectonic evolution of the Los Angeles basin and inner California borderland: A model for core complex-like crustal extension. *Geological Society of America Bulletin*, *105*(11), 1415–1434. https://doi.org/10.1130/0016-7606(1993)105<1415:lcteot>2.3.co;2

Dartnell, P., & Gardner, J. V. (2009). Seafloor terrain analysis and geomorphology of the greater Los Angeles Margin and San Pedro Basin, Southern California. In *Earth science in the urban ocean: The Southern California continental borderland* (Vol. 454, pp. 9).

DeLong, S. B., Hilley, G. E., Rymer, M. J., & Prentice, C. (2010). Fault zone structure from topography: Signatures of en echelon fault slip at Mustang Ridge on the San Andreas Fault, Monterey County, California. *Tectonics*, *29*(5), 16. https://doi.org/10.1029/2010tc002673

Dondurur, D. (2018). *Acquisition and processing of marine seismic data*. Elsevier.

Dooley, T., & McClay, K. (1997). Analog modeling of pull-apart basins. *AAPG Bulletin*, *81*(11), 1804–1826. https://doi.org/10.1306/3b05c636-172a-11d7-8645000102c1865d

Dooley, T. P., & Schreurs, G. (2012). Analogue modelling of intraplate strike-slip tectonics: A review and new experimental results. *Tectonophysics*, *574*, 1–71. https://doi.org/10.1016/j.tecto.2012.05.030

Dunham, E. M., Belanger, D., Cong, L., & Kozdon, J. E. (2011). Earthquake ruptures with strongly rate-weakening friction and off-fault plasticity, Part 1: Planar faults. *Bulletin of the Seismological Society of America*, *101*(5), 2296–2307. https://doi.org/10.1785/0120100075

Efron, B., & Tibshirani, R. J. (1994). *An introduction to the bootstrap*. CRC Press.

Faulkner, D. R., Jackson, C. A. L., Lunn, R. J., Schlische, R. W., Shipton, Z. K., Wibberley, C. A. J., & Withjack, M. O. (2010). A review of recent developments concerning the structure, mechanics and fluid flow properties of fault zones. *Journal of Structural Geology*, *32*(11), 1557–1575. https://doi.org/10.1016/j.jsg.2010.06.009

Faulkner, D. R., Mitchell, T. M., Jensen, E., & Cembrano, J. (2011). Scaling of fault damage zones with displacement and the implications for fault growth processes. *Journal of Geophysical Research*, *116*(B5), B05403. https://doi.org/10.1029/2010JB007788

Fialko, Y. (2002). Deformation on nearby faults induced by the 1999 hector mine earthquake. *Science*, *297*(5588), 1858–1862. https://doi.org/10.1126/science.1074671

Fialko, Y. (2004). Evidence of fluid-filled upper crust from observations of postseismic deformation due to the 1992 M_w7.3 Landers earthquake. *Journal of Geophysical Research*, *109*(B8), B08401. https://doi.org/10.1029/2004jb002985

Fisher, M. A., Normark, W. R., Langenheim, V. E., Calvert, A. J., & Sliter, R. (2004). The offshore Palos Verdes fault zone near san Pedro, southern California. *Bulletin of the Seismological Society of America*, *94*(2), 506–530. https://doi.org/10.1785/0120030042

Fossen, H., & Tikoff, B. (1993). The deformation matrix for simultaneous simple shearing, pure shearing and volume change, and its application to transpression-transtension tectonics. *Journal of Structural Geology*, *15*(3–5), 413–422. https://doi.org/10.1016/0191-8141(93)90137-y

Gardner, J. V., Hughes Clarke, J. E., & Mayer, L. A. (1999). *Cruise report; RV Coastal Surveyor cruise C1-99; Multibeam mapping of the Long Beach California Continental Shelf; April 12, through May 19, 1999*. OF 99-0360. US Geological Survey.

Gazdag, J. (1978). Wave equation migration with the phase-shift method. *Geophysics*, *43*(7), 1342–1351. https://doi.org/10.1190/1.1440899

Guo, H., Brodsky, E., Goebel, T., & Cladouhos, T. (2021). Measuring fault zone and Host rock hydraulic properties using tidal responses. *Geophysical Research Letters*, *48*(13), e2021GL093986. https://doi.org/10.1029/2021gl093986

Hale, D. (2009). Structure-oriented smoothing and semblance. *CWP Report*, *635*(635).

Hale, D. (2013). Methods to compute fault images, extract fault surfaces, and estimate fault throws from 3D seismic images. *Geophysics*, *78*(2), O33–O43. https://doi.org/10.1190/geo2012-0331.1

Huang, Y., Ampuero, J.-P., & Helmberger, D. V. (2014). Earthquake ruptures modulated by waves in damaged fault zones. *Journal of Geophysical Research: Solid Earth*, *119*(4), 3133–3154. https://doi.org/10.1002/2013jb010724

Hubbert, M. K., & Rubey, W. W. (1959). Role of fluid pressure in mechanics of overthrust faulting. Mechanics of fluid-filled porous solids and its application to overthrust faulting. *GSA Bulletin*, *70*(2), 115–166.

Iacopini, D., Butler, R. W. H., Purves, S., McArdle, N., & De Freslon, N. (2016). Exploring the seismic expression of fault zones in 3D seismic volumes. *Journal of Structural Geology*, *89*, 54–73. https://doi.org/10.1016/j.jsg.2016.05.005

Kame, N., Rice, J. R., & Dmowska, R. (2003). Effects of prestress state and rupture velocity on dynamic fault branching. *Journal of Geophysical Research*, *108*(B5), 2265. https://doi.org/10.1029/2002jb002189

Kanamori, H., & Brodsky, E. E. (2004). The physics of earthquakes. *Reports on Progress in Physics*, *67*(8), 1429–1496. https://doi.org/10.1088/0034-4885/67/8/r03

Ke, C.-Y., McLaskey, G. C., & Kammer, D. S. (2022). Earthquake breakdown energy scaling despite constant fracture energy. *Nature Communications*, *13*(1), 1005. https://doi.org/10.1038/s41467-022-28647-4

Kluesner, J., Brothers, D., Hart, P., Miller, N., & Hatcher, G. (2019). Practical approaches to maximizing the resolution of sparker seismic reflection data. *Marine Geophysical Research*, *40*(3), 279–301. https://doi.org/10.1007/s11001-018-9367-2

Kluesner, J. W., & Brothers, D. S. (2016). Seismic attribute detection of faults and fluid pathways within an active strike-slip shear zone: New insights from high-resolution 3D P-Cable™ seismic data along the Hosgri Fault, offshore California. *Interpretation*, *4*(1), SB131–SB148. https://doi.org/10.1190/INT-2015-0143.1

Kluesner, J. W., Silver, E. A., Bangs, N. L., McIntosh, K. D., Gibson, J., Orange, D., et al. (2013). High density of structurally controlled, shallow to deep water fluid seep indicators imaged offshore Costa Rica. *Geochemistry, Geophysics, Geosystems*, *14*(3), 519–539. https://doi.org/10.1002/ggge.20058

Kurzon, I., Vernon, F. L., Ben-Zion, Y., & Atkinson, G. (2014). Ground motion prediction equations in the San Jacinto fault zone: Significant effects of rupture directivity and fault zone amplification. *Pure and Applied Geophysics*, *171*(11), 3045–3081. https://doi.org/10.1007/s00024-014-0855-2

Li, Y. G., Catchings, R. D., & Goldman, M. R. (2016). Subsurface fault damage zone of the 2014 M w 6.0 South Napa, California, earthquake viewed from fault-zone trapped waves. *Bulletin of the Seismological Society of America*, *106*(6), 2747–2763. https://doi.org/10.1785/0120160039

Li, Y.-G., Ellsworth, W. L., Thurber, C. H., Malin, P. E., & Aki, K. (1997). Fault-zone guided waves from explosions in the San Andreas Fault at Parkfield and Cienega Valley, California. *Bulletin of the Seismological Society of America*, *87*(1), 210–221. https://doi.org/10.1785/bssa0870010210

Li, Y.-G., Vidale, J. E., & Cochran, E. S. (2004). Low-velocity damaged structure of the San Andreas Fault at Parkfield from fault zone trapped waves. *Geophysical Research Letters*, *31*(12), n/a. https://doi.org/10.1029/2003GL019044

Liao, Z., Hu, L., Huang, X., Carpenter, B. M., Marfurt, K. J., Vasileva, S., & Zhou, Y. (2020). Characterizing damage zones of normal faults using seismic variance in the Wangxuzhuang oilfield, China. *Interpretation*, *8*(4), SP53–SP60. https://doi.org/10.1190/int-2020-0004.1

Liao, Z., Liu, H., Carpenter, B. M., Marfurt, K. J., & Reches, Z. (2019). Analysis of fault damage zones using three-dimensional seismic coherence in the Anadarko Basin, Oklahoma. *AAPG Bulletin*, *103*(8), 1771–1785. https://doi.org/10.1306/1219181413417207

Løseth, H., Gading, M., & Wensaas, L. (2009). Hydrocarbon leakage interpreted on seismic data. *Marine and Petroleum Geology*, *26*(7), 1304–1319. https://doi.org/10.1016/j.marpetgeo.2008.09.008

Ma, D.-B., Wu, G.-H., Scarselli, N., Luo, X.-S., Han, J.-F., & Chen, Z.-Y. (2019). Seismic damage zone and width–throw scaling along the strike-slip faults in the Ordovician carbonates in the Tarim Basin. *Petroleum Science*, *16*(4), 752–762. https://doi.org/10.1007/s12182-019-0352-4

Mann, P. (2007). Global catalogue, classification and tectonic origins of restraining-and releasing bends on active and ancient strike-slip fault systems. *Geological Society, London, Special Publications*, *290*(1), 13–142. https://doi.org/10.1144/sp290.2

Marfurt, K. J., Kirlin, R. L., Farmer, S. L., & Bahorich, M. S. (1998). 3-D seismic attributes using a semblance-based coherency algorithm. *Geophysics*, *63*(4), 1150–1165. https://doi.org/10.1190/1.1444415

Martel, S. J., & Pollard, D. D. (1989). Mechanics of slip and fracture along small faults and simple strike-slip fault zones in granitic rock. *Journal of Geophysical Research*, *94*(B7), 9417–9428. https://doi.org/10.1029/JB094iB07p09417

Materna, K., & Bürgmann, R. (2016). Contrasts in compliant fault zone properties inferred from geodetic measurements in the San Francisco Bay area. *Journal of Geophysical Research: Solid Earth*, *121*(9), 6916–6931. https://doi.org/10.1002/2016JB013243

McClay, K., & Bonora, M. (2001). Analog models of restraining stepovers in strike-slip fault systems. *AAPG Bulletin*, *85*(2), 233–260. https://doi.org/10.1306/8626c7ad-173b-11d7-8645000102c1865d

McNeilan, T. W., Rockwell, T. K., & Resnick, G. S. (1996). Style and rate of Holocene slip, Palos Verdes fault, southern California. *Journal of Geophysical Research*, *101*(B4), 8317–8334. https://doi.org/10.1029/95JB02251

Milliner, C., Donnellan, A., Aati, S., Avouac, J.-P., Zinke, R., Dolan, J. F., et al. (2021). Bookshelf kinematics and the effect of dilatation on fault zone inelastic deformation: Examples from optical image correlation measurements of the 2019 Ridgecrest earthquake sequence. *Journal of Geophysical Research: Solid Earth*, *126*(3), e2020JB020551. https://doi.org/10.1029/2020jb020551

Naylor, M., Mandl, G. T., & Supesteijn, C. (1986). Fault geometries in basement-induced wrench faulting under different initial stress states. *Journal of Structural Geology*, *8*(7), 737–752. https://doi.org/10.1016/0191-8141(86)90022-2

OpendTect. (2022). (Version 6.0) [Computer Software]. Retrieved from https://dbges.com

Platt, J. P., & Becker, T. W. (2010). Where is the real transform boundary in California? *Geochemistry, Geophysics, Geosystems*, *11*(6), Q06012. https://doi.org/10.1029/2010gc003060

Pollard, D., Segall, P., & Atkinson, B. (1987). Fracture mechanics of rock. In *Theoretical displacements and stresses near fractures in rock: With applications to faults, joints, veins, dikes, and solution surfaces* (pp. 277–349). Academic Press.

Prouty, N. G., Brothers, D. S., Kluesner, J. W., Barrie, J. V., Andrews, B. D., Lauer, R. M., et al. (2020). Focused fluid flow and methane venting along the Queen Charlotte fault, offshore Alaska (USA) and British Columbia (Canada). *Geosphere*, *16*(6), 1336–1357. https://doi.org/10.1130/ges02269.1

Qiu, H., Ben-Zion, Y., Catchings, R., Goldman, M. R., Allam, A. A., & Steidl, J. (2021). Seismic imaging of the Mw 7.1 Ridgecrest earthquake rupture zone from data recorded by dense linear arrays. *Journal of Geophysical Research: Solid Earth*, *126*(7), e2021JB022043. https://doi.org/10.1029/2021jb022043

Reveal. (2022). (Version 4 and 5) [Computer Software]. Retrieved from https://reveal.shearwatergeo.com/

Rigor, A. W. (2003). Structure and deformation of the Palos Verdes fault in San Pedro Bay, California [PhD Thesis]. San Diego State University.

Rodriguez Padilla, A. M., Oskin, M. E., Milliner, C. W., & Plesch, A. (2022). Accrual of widespread rock damage from the 2019 Ridgecrest earthquakes. *Nature Geoscience*, *15*(3), 222–226. https://doi.org/10.1038/s41561-021-00888-w

Rudebusch, J. A., Prouty, N. G., Conrad, J. E., Watt, J. T., Kluesner, J., Hill, J. C., et al. (2023). Diving deeper into seep distribution along the Cascadia Convergent Margin, USA. *Frontiers in Earth Science*, *11*, 1205211. https://doi.org/10.3389/feart.2023.1205211

Sanderson, D. J., & Marchini, W. (1984). Transpression. *Journal of Structural Geology*, *6*(5), 449–458. https://doi.org/10.1016/0191-8141(84)90058-0

Savage, H. M., & Brodsky, E. E. (2011). Collateral damage: Evolution with displacement of fracture distribution and secondary fault strands in fault damage zones. *Journal of Geophysical Research*, *116*(B3), B03405. https://doi.org/10.1029/2010JB007665

Scott, C. P., Arrowsmith, J. R., Nissen, E., Lajoie, L., Maruyama, T., & Chiba, T. (2018). The M 7 2016 Kumamoto, Japan, Earthquake: 3-D deformation along the fault and within the damage zone constrained from differential lidar topography. *Journal of Geophysical Research: Solid Earth*, *123*(7), 6138–6155. https://doi.org/10.1029/2018JB015581

Scott, C. P., DeLong, S. B., & Arrowsmith, J. R. (2020). Distribution of aseismic deformation along the Central San Andreas and Calaveras faults from differencing repeat airborne lidar. *Geophysical Research Letters*, *47*(22), e2020GL090628. https://doi.org/10.1029/2020gl090628

Segall, P. (2010). *Earthquake and volcano deformation*. Princeton University Press.

Segall, P., & Pollard, D. (1980). Mechanics of discontinuous faults. *Journal of Geophysical Research*, *85*(B8), 4337–4350. https://doi.org/10.1029/jb085ib08p04337

Sheriff, R. E., & Geldart, L. P. (1995). *Exploration seismology*. Cambridge University Press.

Shipton, Z. K., & Cowie, P. A. (2001). Damage zone and slip-surface evolution over μm to km scales in high-porosity Navajo sandstone, Utah. *Journal of Structural Geology*, *23*(12), 1825–1844.

Sorlien, C. C., Seeber, L., Broderick, K. G., Luyendyk, B. P., Fisher, M. A., Sliter, R. W., & Normark, W. R. (2013). The Palos Verdes anticlinorium along the Los Angeles, California coast: Implications for underlying thrust faulting. *Geochemistry, Geophysics, Geosystems*, *14*(6), 1866–1890. https://doi.org/10.1002/ggge.20112

Spudich, P., & Olsen, K. (2001). Fault zone amplified waves as a possible seismic hazard along the Calaveras fault in central California. *Geophysical Research Letters*, *28*(13), 2533–2536. https://doi.org/10.1029/2000gl011902

Suess, E. (2020). Marine cold seeps: Background and recent advances. In *Hydrocarbons, oils and lipids: Diversity, origin, chemistry and fate* (pp. 747–767).

Sylvester, A. G. (1988). Strike-slip faults. *Geological Society of America Bulletin*, *100*(11), 1666–1703. https://doi.org/10.1130/0016-7606(1988)100<1666:ssf>2.3.co;2

Tada, H., Paris, P. C., & Irwin, G. R. (1973). *The stress analysis of cracks. Handbook* (Vol. 34). Del Research Corporation.

Teran, O. J., Fletcher, J. M., Oskin, M. E., Rockwell, T. K., Hudnut, K. W., Spelz, R. M., et al. (2015). Geologic and structural controls on rupture zone fabric: A field-based study of the 2010 Mw 7.2 El Mayor–Cucapah earthquake surface rupture. *Geosphere*, *11*(3), 899–920. https://doi.org/10.1130/ges01078.1

Thakur, P., Huang, Y., & Kaneko, Y. (2020). Effects of low-velocity fault damage zones on long-term earthquake behaviors on mature strike-slip faults. *Journal of Geophysical Research: Solid Earth*, *125*(8), e2020JB019587. https://doi.org/10.1029/2020JB019587

Thurber, C., Roecker, S., Ellsworth, W., Chen, Y., Lutter, W., & Sessions, R. (1997). Two-dimensional seismic image of the San Andreas Fault in the Northern Gabilan Range, central California: Evidence for fluids in the fault zone. *Geophysical Research Letters*, *24*(13), 1591–1594. https://doi.org/10.1029/97GL01435

Tingdahl, K. M., & De Rooij, M. (2005). Semi-automatic detection of faults in 3D seismic data. *Geophysical Prospecting*, *53*(4), 533–542. https://doi.org/10.1111/j.1365-2478.2005.00489.x

Torabi, A., & Berg, S. S. (2011). Scaling of fault attributes: A review. *Marine and Petroleum Geology*, *28*(8), 1444–1460. https://doi.org/10.1016/j.marpetgeo.2011.04.003

Torabi, A., Ellingsen, T., Johannessen, M., Alaei, B., Rotevatn, A., & Chiarella, D. (2020). Fault zone architecture and its scaling laws: Where does the damage zone start and stop? *Geological Society, London, Special Publications*, *496*(1), 99–124. https://doi.org/10.1144/sp496-2018-151

Tréhu, A. M., Torres, M. E., Moore, G. F., Suess, E., & Bohrmann, G. (1999). Temporal and spatial evolution of a gas hydrate–bearing accretionary ridge on the Oregon continental margin. *Geology*, *27*(10), 939–942. https://doi.org/10.1130/0091-7613(1999)027<0939:taseoa>2.3.co;2

Triezenberg, P., Hart, P., & Childs, J. (2016). *National Archive of Marine Seismic Surveys (NAMSS)—A USGS data website of marineseismic reflection data within the U.S. exclusive economic zone (EEZ)*. U.S. Geological Survey. Retrieved from https://walrus.wr.usgs.gov/NAMSS/

Uieda, L., Tian, D., Leong, W. J., Toney, L., Schlitzer, W., Grund, M., et al. (2021). PyGMT: A Python interface for the generic mapping tools.

Verschuur, D. J., Berkhout, A., & Wapenaar, C. (1992). Adaptive surface-related multiple elimination. *Geophysics*, *57*(9), 1166–1177. https://doi.org/10.1190/1.1443330

Walton, M. A., Brothers, D. S., Conrad, J. E., Maier, K. L., Roland, E. C., Kluesner, J. W., & Dartnell, P. (2020). Morphology, structure, and kinematics of the San Clemente and Catalina faults based on high-resolution marine geophysical data, southern California Inner Continental Borderland (USA). *Geosphere*, *16*(5), 1312–1335. https://doi.org/10.1130/ges02187.1

Walton, M. A., Papesh, A., Johnson, S., & Brothers, D. (2020). *Quaternary faults offshore of California*. U.S. Geological Survey Data Release. https://doi.org/10.5066/P91RYEZ4

Ward, S. N., & Valensise, G. (1994). The Palos Verdes terraces, California: Bathtub rings from a buried reverse fault. *Journal of Geophysical Research*, *99*(B3), 4485–4494. https://doi.org/10.1029/93JB03362

Wessel, P., Luis, J. F., Uieda, L. A., Scharroo, R., Wobbe, F., Smith, W. H., & Tian, D. (2019). The generic mapping tools version 6. *Geochemistry, Geophysics, Geosystems*, *20*(11), 5556–5564. https://doi.org/10.1029/2019gc008515

White, M. C., Fang, H., Catchings, R. D., Goldman, M. R., Steidl, J. H., & Ben-Zion, Y. (2021). Detailed traveltime tomography and seismic catalogue around the 2019 M w7. 1 Ridgecrest, California, earthquake using dense rapid-response seismic data. *Geophysical Journal International*, *227*(1), 204–227. https://doi.org/10.1093/gji/ggab224

Wolfe, F. D., Shaw, J. H., & Plesch, A. (2022). Origin of the Palos Verdes restraining bend and its implications for the 3D geometry of the Fault and earthquake hazards in Los Angeles, California. *Bulletin of the Seismological Society of America*, *112*(5), 2689–2714. https://doi.org/10.1785/0120210278

Wong, T. (1982). Shear fracture energy of Westerly granite from post-failure behavior. *Journal of Geophysical Research*, *87*(B2), 990–1000. https://doi.org/10.1029/JB087iB02p00990

Wright, T. (1991). Active margin basins. In *American Association of Petroleum Geologists Memoir 52* (pp. 35–134).

Wu, C., Peng, Z., & Ben-Zion, Y. (2009). Non-linearity and temporal changes of fault zone site response associated with strong ground motion. *Geophysical Journal International*, *176*(1), 265–278. https://doi.org/10.1111/j.1365-246x.2008.04005.x

Xu, X., Liu, D., & Lavier, L. (2023). Constraining fault damage zone properties from geodesy: A case study near the 2019 Ridgecrest earthquake sequence. *Geophysical Research Letters*, *50*(5), e2022GL101692. https://doi.org/10.1029/2022gl101692

Yang, H., Li, Z., Peng, Z., Ben-Zion, Y., & Vernon, F. (2014). Low-velocity zones along the San Jacinto Fault, Southern California, from body waves recorded in dense linear arrays: Damage zones of the San Jacinto Fault. *Journal of Geophysical Research: Solid Earth*, *119*(12), 8976–8990. https://doi.org/10.1002/2014JB011548

Yang, H., Zhu, L., & Cochran, E. S. (2011). Seismic structures of the Calico fault zone inferred from local earthquake travel time modelling: Seismic structures of the Calico fault zone. *Geophysical Journal International*, *186*(2), 760–770. https://doi.org/10.1111/j.1365-246X.2011.05055.x

Yeats, R. S., & Beall, J. M. (1991). Stratigraphic controls of oil fields in the Los Angeles basin a guide to migration history. Chapter 7.

Yilmaz, Ö. (2001). *Seismic data analysis: Processing, inversion, and interpretation of seismic data*. Society of Exploration Geophysicists.

References From the Supporting Information

Cox, M. (1999). *Static corrections for seismic reflection surveys*. Society of Exploration Geophysicists. Retrieved from http://library.seg.org/doi/book/10.1190/1.9781560801818/